

# Enhancing Thermal Interface Conductance to Graphene Using Ni–Pd Alloy Contacts

Dipanjana Saha, Xiaoxiao Yu, Yanhao Du, Zhitao Guo, Feng Xiong, Andrew J. Gellman, and Jonathan A. Malen\*



Cite This: *ACS Appl. Mater. Interfaces* 2020, 12, 34317–34322



Read Online

ACCESS |



Metrics & More



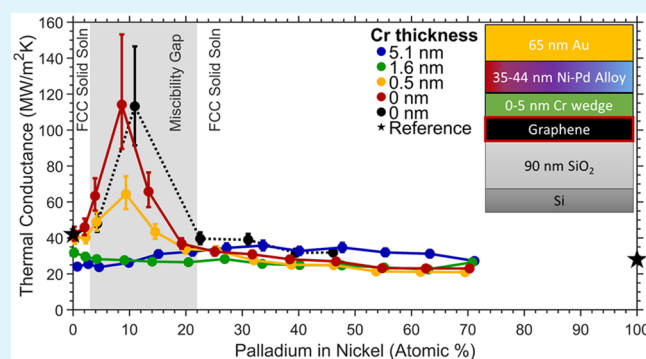
Article Recommendations



Supporting Information

**ABSTRACT:** To identify superior thermal contacts to graphene, we implement a high-throughput methodology that systematically explores the Ni–Pd alloy composition spectrum and the effect of Cr adhesion layer thickness on thermal interface conductance with monolayer graphene. Frequency domain thermoreflectance measurements of two independently prepared Ni–Pd/Cr/graphene/SiO<sub>2</sub> samples identify a maximum metal/graphene/SiO<sub>2</sub> junction thermal interface conductance of  $114 \pm (39, 25)$  MW/m<sup>2</sup> K and  $113 \pm (33, 22)$  MW/m<sup>2</sup> K at ~10 at. % Pd in Ni—nearly double the highest reported value for pure metals and 3 times that of pure Ni or Pd. The presence of Cr, at any thickness, suppresses this maximum. Although the origin of the peak is unresolved, we find that it correlates with a region of the Ni–Pd phase diagram that exhibits a miscibility gap. Cross-sectional imaging by high-resolution transmission electron microscopy identifies striations in the alloy at this particular composition, consistent with separation into multiple phases. Through this work, we draw attention to alloys in the search for better contacts to two-dimensional materials for next-generation devices.

**KEYWORDS:** 2D materials, thermoreflectance, alloy thin films, miscibility gap, TEM images



## INTRODUCTION

Heat dissipation into metal contacts is critical to the high-performance operation of short-channel graphene devices.<sup>1–6</sup> Pure metal thermal contacts to graphene can spread heat laterally, but their poor thermal interface conductance ( $G$ ) is a bottleneck to the removal of heat generated in the graphene channel and at contact interfaces.<sup>7–9</sup> The heat transfer across the metal–graphene interfaces is phonon dominated.<sup>10,11</sup> Alignment of the phonon spectra across the interface is one consideration in the search for high  $G$ . The Debye temperature characterizes the thermal activation of a lattice's highest energy phonons. Graphene has a high Debye temperature of 1287 K,<sup>12</sup> and thus, metals also possessing a high Debye temperature should be favorable thermal contacts. As exhibited in Figure 1 by the spread in  $G$  values for pure metal/graphene/SiO<sub>2</sub> junctions (where the junction is composed of graphene and its two interfaces because an individual interface cannot be resolved),<sup>11,13–15</sup> there are additional factors beyond phonon spectrum alignment. One major factor is the adhesion strength of the metal to graphene. For example, Hopkins et al. were able to double  $G$  by functionalizing the surface of monolayer graphene with oxygen atoms for better bonding to the Al metal contact.<sup>15</sup> Zheng et al. found that the strongly bound TiN contacts offered high thermal interface conductance with graphene and measured a value of 135 MW/m<sup>2</sup> K for the TiN/

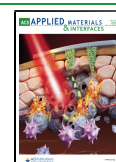
graphene/TiN junction (cannot be compared directly with the metal/graphene/SiO<sub>2</sub> junctions shown in Figure 1).<sup>16</sup> Nonetheless, the inherently low thermal conductivity of TiN thin films (7.5–11 W/m/K<sup>16,17</sup>) may limit their utility as heat spreaders.

Although maximizing adhesion strength may seem desirable, a very strong interaction can result in the metal reacting with the underlying graphene to form a carbide, which is detrimental to the electrical performance of the device.<sup>18</sup> Such a strong interaction is classified as chemisorption (where the metal chemically binds to the graphene) in contrast to physisorption (a weaker interaction where the metal is in physical contact with the graphene). Al, Ag, Cu, Au, Pt, and Cr are metals recognized as physisorbing to graphene; Co, Ti, Ni, and TiN are chemisorbing; and Pd is described in the literature as very weakly chemisorbing/strongly physisorbing.<sup>19–25</sup> These distinctions are based on the binding energy and equilibrium bonding distance between the metal and graphene

Received: April 17, 2020

Accepted: July 1, 2020

Published: July 1, 2020



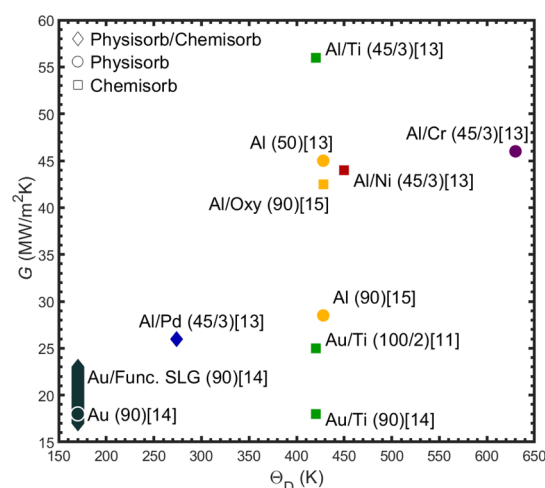


**Figure 1.** Thermal interface conductance ( $G$ ) vs Debye temperature ( $\Theta_D$ ) for junctions composed of metal/monolayer graphene/ $\text{SiO}_2$ .<sup>11,13–15</sup> The plotted  $\Theta_D$  values correspond to that of the metal in contact with the graphene (grouped by colors). Al/oxy refers to an Al thermal contact on oxygen-functionalized monolayer graphene.<sup>15</sup> The range of data for Au/functionalized single-layer graphene (SLG) encompasses functionalization by oxygen, fluorine, and nitrogen to varying degrees of graphene surface coverage.<sup>14</sup> The values in parentheses denote the thicknesses of metals and adhesion layers in nanometers. Circles denote physisorbing metal/SLG interactions, squares denote chemisorbing interactions, and diamond denotes intermediary interactions.<sup>19–25</sup>

as calculated by the first-principles density functional theory methods.<sup>20</sup>

The limited choice of pure metals motivates research into whether alloy composition can tune the interaction strength to optimize the interfacial heat transport. The ideal interaction would maximize adhesion without damaging the graphene for electrical applications. Unfortunately, optimization studies of alloy contacts to graphene are complicated by the overwhelming nature of the alloy design space.

An additional design consideration is adhesion layer thickness, which has major implications for thermal transport. For example, Jeong et al. reported that  $G$  between Au and  $\text{Al}_2\text{O}_3$  increased from  $60 \pm 10$  to  $300 \pm 50 \text{ MW/m}^2 \text{ K}$  as the thickness of a Cr adhesion layer increased from 0 to 1 nm.<sup>26</sup> For reference, the two most common graphene adhesion layers, Cr and Ti, are used with thicknesses spanning from 0.5 to 10 nm according to the electrical graphene contact resistance literature.<sup>6,27–31</sup> Clearly, a lack of consensus exists as far as the optimal adhesion layer thickness for graphene contacts is concerned.

Utilizing high-throughput techniques, we define and implement a new methodology to systematically investigate the relatively unexplored frontier of alloy–graphene contacts, as well as the effect of adhesion layer thickness on  $G$ . Specifically, we present measurements of  $G$  as a function of alloy composition for a Ni–Pd alloy and thickness for a Cr adhesion layer. Ni–Pd alloys were studied because the spectrum of chemisorption (Ni) to strong physisorption (Pd) is represented. Additionally, Ni and Pd are two of the best electrical graphene contacts.<sup>29</sup>

With this initial study, we find that  $\sim 10$  at. % Pd in Ni without an adhesion layer yields a maximum thermal interface conductance of  $114 \pm (39, 25) \text{ MW/m}^2 \text{ K}$ , which is double the value of the next highest reported  $G$  for a metal/graphene/

$\text{SiO}_2$  junction.<sup>13</sup> This major enhancement in  $G$  only requires the up-front complexity associated with depositing alloys via evaporation, either by coevaporation of alloy constituents<sup>32</sup> or by evaporation from an alloy target.<sup>33,34</sup> By comparison, other enhancement techniques such as functionalizing the graphene surface achieved 38% of our maximum  $G$ <sup>15</sup> but can impede electrical transport from the metal to the graphene.<sup>14</sup> Although the physics underlying our large  $G$  is not yet understood, we observe a clear correlation between the alloy composition where enhancement of  $G$  occurs and the existence of a miscibility gap in the alloy phase diagram.

## RESULTS AND DISCUSSION

High-throughput thermal interface conductance data acquisition is possible by first depositing a Cr metal wedge adhesion layer, 0–5 nm in thickness, onto graphene on 90 nm  $\text{SiO}_2$  on Si. Subsequently, opposing Ni and Pd wedges are codeposited to produce a metal contact of 35–44 nm thickness with alloy composition varying spatially across the lateral dimension of the sample. Capping the sample with a Au transducer layer enables the sample to be scanned spatially using the laser pump/probe technique, frequency domain thermoreflectance (FDTR), to measure  $G$  as a function of adhesion layer thickness and alloy composition, as determined by energy-dispersive X-ray (EDX) spectroscopy. Sinusoidal modulation of the pump laser creates a periodic temperature change in the sample with an amplitude and phase, relative to the pump, that depend on the unknown value of  $G$ . The temperature response is measured by the probe laser via thermoreflectance, and the phase data are fit over a range of modulation frequencies with an analytical solution to the heat diffusion equation in order to determine  $G$ .<sup>37</sup> The FDTR phase data and fits are plotted in the inset of Figure 2 as a function of frequency for 8 and 70 at. % Pd, illustrating the goodness of fit and its sensitivity to  $G$ .

As with the literature values shown in Figure 1, the values of  $G$  plotted in Figure 2 represent that of the junction composed of monolayer graphene and its two adjacent interfaces (i.e., the metal/graphene/ $\text{SiO}_2$  junction highlighted in red in the inset). In the regions where the Cr adhesion layer is the thickest (1.6–5.1 nm), no significant effects of Ni–Pd composition on  $G$  are observed. These Cr thicknesses apparently dampen any alloy–graphene interaction. However, measurements of  $G$  corresponding to a Cr thickness of 0.5 nm (2–3 atomic layers of Cr) show an increase in  $G$  at  $\sim 8$  at. % Pd in Ni. Most notably, measurements taken in the region where the Ni–Pd alloy is directly in contact with the graphene (not Cr) exhibit a maximum  $G$  of  $114 \pm (39, 25) \text{ MW/m}^2 \text{ K}$ . Such a large  $G$  is double the highest reported thermal interface conductance for a pure metal/monolayer graphene/ $\text{SiO}_2$  junction (see the Al/Ti contact in Figure 1).<sup>13</sup> Our measurements of 0 at. % Pd and 70 at. % Pd compare well with the reference values for pure Ni/graphene/ $\text{SiO}_2$  and Pd/graphene/ $\text{SiO}_2$  junctions (within 10%).<sup>13</sup> The highest values of  $G$  that we observe for Cr/graphene/ $\text{SiO}_2$  are 20% lower than those previously reported for Cr/graphene/ $\text{SiO}_2$ .<sup>13</sup> As evidenced by the range of  $G$  we see as a function of Pd content and Cr thickness, this may occur because of the interdiffusion driven by the annealing process (in ref 13, Cr is capped with Al and the films are not annealed).<sup>38</sup>

Because of the surprising appearance of a peak in  $G$  at an intermediate Ni–Pd composition, a second sample without a Cr adhesion layer was fabricated to verify reproducibility (black circles). This second sample does not include a Cr

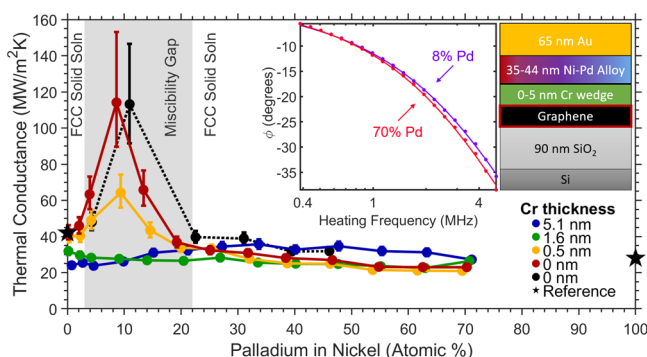


**Figure 2.** FDTR measurements of thermal interface conductance ( $G$ ) as a function of Ni–Pd alloy composition and Cr thickness (colored lines). The material stack is shown in the top right inset, where  $G$  across the metal/graphene/ $\text{SiO}_2$  junction (outlined in red) is reported. A peak in  $G$  is observed for zero adhesion layer thickness (red circles), a trend well reproduced by a second sample with no Cr adhesion layer (black circles). A smaller peak is also observable for 0.5 nm of Cr (yellow circles), where the peak value is suppressed relative to 0 nm of Cr. The emergence of the peak clearly correlates with the composition range over which the alloy phase diagram exhibits a miscibility gap (gray-shaded region) based on the binary phase diagram calculated for an annealing temperature of 180 °C.<sup>35,36</sup> The data also show good agreement with the pure metal reference values<sup>13</sup> (black stars, also shown in Figure 1), if measured data is extrapolated to pure Pd. The vertical error bars represent the first and third quartiles in the distribution of  $G$  resulting from uncertainty propagation in the FDTR fitting parameters (further details are given in the Supporting Information). The horizontal error bars estimated as  $\pm 2$  at. % Pd in Ni are not shown for legibility. The top central inset shows a clear difference in the phase lag versus frequency thermoreflectance data at the peak conductance alloy composition as compared to 70% Pd in Ni for 0 nm thickness of Cr.

adhesion layer because it only suppresses the peak in conductance. A peak of similar magnitude,  $G = 113 \pm (33, 22)$   $\text{MW/m}^2 \text{K}$ , is observed for the second sample at a similar composition of 11 at. % Pd. While some minor misalignment (as a function of alloy composition) in the peaks of the two data sets is observable, this can be attributed to the positions of the EDX spectroscopy and thermal measurements not being perfectly colocated. Horizontal error bars on the data, estimated as  $\pm 2$  at. % Pd in Ni, are not shown in Figure 2 for legibility. Nevertheless, these two separate samples demonstrate that a peak in  $G$  exists for  $\sim 10$  at. % Pd in Ni alloy directly in contact with monolayer graphene on  $\text{SiO}_2$ . Although the physical origin of the enhancement in  $G$  is unresolved, we find that the peak and its less-enhanced neighboring points (red circles) occur at compositions of Ni–Pd, where there exists a miscibility gap in the binary phase diagram at our film annealing temperature of 180 °C (Figure S1 in the Supporting Information depicts the Ni–Pd binary alloy phase diagram<sup>35,36</sup>). The same phenomena are also observed for 0.5 nm of Cr as an adhesion layer (yellow circles).

The existence of a miscibility gap in the Ni–Pd system itself has been historically contentious due to contradicting experimental observations.<sup>39–42</sup> For this reason, we present cross-sectional high-resolution transmission electron microscopy (HRTEM) images of the contacts at  $\sim 8$  at. % Pd in Ni, the composition of the maximum  $G$ . For comparison, the cross-sectional HRTEM images were also taken at  $\sim 60$  at. % Pd. These HRTEM images are shown in Figure 3. In Figure 3a, striated areas circled in yellow identify the alloy as phase

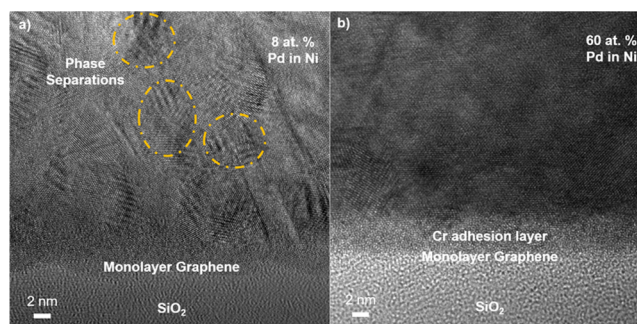


**Figure 3.** a) Cross-sectional HRTEM image of 8 at. % Pd in Ni on monolayer graphene on  $\text{SiO}_2$ . The graphene itself is not visible, but its relative location in conformance with the  $\text{SiO}_2$  morphology is shown. Circled in yellow are three of the multiple regions with visible striations associated with phase separations of the Ni–Pd alloy, demonstrating that the alloy at this composition is in a miscibility gap. (b) For comparison, HRTEM image from a sample region where enhancement in  $G$  is not observed. Phase separation is not apparent at a composition of 60 at. % Pd in Ni with a 2 nm Cr adhesion layer.

separating, which compare well with the images of phase-separated alloys (characterized as spinodal decompositions) presented in the work of Androulakis et al.<sup>43</sup> The physical characteristics of the phase-separated regions, such as the striation wavelength, depend on the thermal treatment conditions of the alloy.<sup>44</sup> Similar striations are not apparent in the  $\sim 60$  at. % Pd image shown in Figure 3b. If the miscibility gap is responsible for the enhancement of  $G$ , then the observed enhancement would not be expected at higher operating temperatures where the alloy phase is a solid solution (i.e., greater than 550 K).

Figure 3 does not visualize the monolayer graphene directly, and thus, we cannot rule out the hypothesis that the peak in  $G$  results from the pinholes in the graphene that would allow direct contact between the Ni–Pd alloy and  $\text{SiO}_2$ . This hypothesis is motivated by Leong et al., who showed that annealing Ni-containing contacts can etch the underlying graphene.<sup>45,46</sup> Direct measurements of  $G$  at the interface between Pd and  $\text{SiO}_2$  have not been published, but for reference, a recently reported value of  $G$  of Pt on  $\text{SiO}_2$  is 300  $\text{MW/m}^2 \text{K}$ .<sup>47</sup> Thus, parallel heat transfer through (1) pinholes allowing direct alloy/ $\text{SiO}_2$  contact and (2) across the targeted alloy/graphene/ $\text{SiO}_2$  junction is a possible cause of the observed enhancement. However, this mechanism would also be expected to produce enhanced  $G$  for pure Ni, which we do not observe. Cross-sectional HRTEM imaging of monolayer graphene has historically been difficult. For example, Norimatsu and Kusunoki were successful in imaging SLG on SiC with a buffer layer,<sup>48</sup> whereas other attempts were not.<sup>49–52</sup> Therefore, the inability to visualize the graphene by our HRTEM imaging should not be prematurely concluded to indicate that it has been compromised relative to its high-quality monolayer state prior to metal deposition, as verified by Raman spectroscopy (see Figure S6 in the Supporting Information).

## CONCLUSIONS

Utilizing high-throughput techniques, we find that Ni–Pd alloy contacts to graphene exhibit a value of  $G$  that is nearly double that of any pure metal contact and over 3 times that of pure Ni or Pd. The composition of maximum  $G$ ,  $\sim 10$  at. % Pd in Ni, clearly correlates with a miscibility gap in the Ni–Pd binary

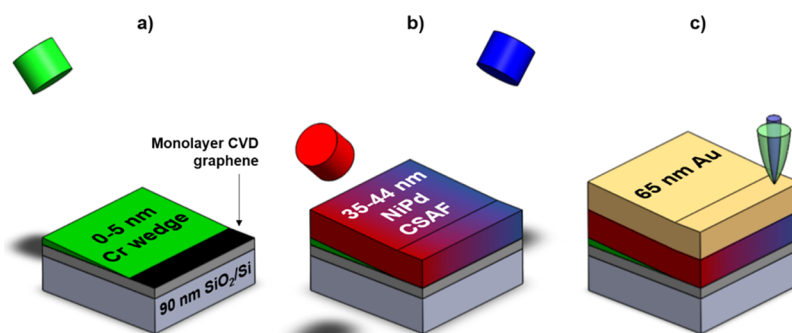


**Figure 4.** Sample fabrication sequence. (a) First, a 0–5 nm Cr wedge is deposited onto monolayer CVD graphene/90 nm SiO<sub>2</sub>/Si. (b) In the perpendicular direction, Ni and Pd wedges are codeposited to form a 35–44 nm CSAF. (c) Final capping with a 65 nm Au film needed for FDTR measurements where coaligned blue and green lasers scan across the sample to measure  $G$  as a function of alloy composition and Cr adhesion layer thickness.

phase diagram. In comparison, the phases of compositions outside of the miscibility gap where  $G$  is not enhanced are face-centered cubic solid solutions.<sup>35,36</sup> HRTEM imaging of the peak  $G$  alloy composition identify striations that confirm the phase separation of the alloy in agreement with the miscibility gap region of the binary alloy phase diagram, the existence of which was previously debated. Although the origin of enhanced  $G$  is unknown, this work demonstrates the potential for engineered alloys to form better thermal contacts to two-dimensional materials than pure metals. If the observed peak in  $G$  results from better adhesion to graphene or the creation of pinholes, both of which would be expected to enhance electrical transport,<sup>53</sup> then depositing  $\sim 10$  at. % Pd in Ni as the metal contact is a simple method to advance high-performance graphene electronics. Further research is required to understand the origin of the enhanced  $G$  and whether alloy composition represents a general tool for engineering other interfacial transport properties, such as electrical contact conductance.

## METHODS

**Graphene Acquisition.** The samples consist of chemical vapor deposition (CVD)-grown monolayer graphene transferred to 90 nm of SiO<sub>2</sub> on Si, acquired from the commercial supplier Graphene Supermarket. Prior to metal deposition, the samples are first annealed at 250 °C for 4 h in 5% H<sub>2</sub> in Ar by volume (25 sccm H<sub>2</sub> in 475 sccm of Ar in a 2" diameter quartz tube) at atmospheric pressure. Annealing in H<sub>2</sub>/Ar is a common approach to remove organic contaminants from the graphene surface.<sup>54,55</sup> Although some polymer residues can still remain,<sup>56</sup> more aggressive surface cleaning techniques present significant risk to damaging the graphene.<sup>27</sup> Raman spectroscopy following the H<sub>2</sub>/Ar annealing procedure validates the graphene to be of sufficiently high quality and monolayer (see Figure S6 in the Supporting Information).

**Compositionally Spread Alloy Film Deposition.** The metal deposition process onto the annealed graphene involves three steps diagrammed in Figure 4. First, a Cr wedge is deposited ranging in thickness from 0 to 5 nm. Next, in the perpendicular direction of the Cr thickness gradient, Ni and Pd wedges are codeposited to create an alloy film with composition varying as a function of space—known as a compositionally spread alloy film (CSAF).<sup>57,58</sup> Thus, with one sample, a high-throughput study probing an entire spectrum of alloy compositions can be conducted instead of numerous samples with discrete alloy compositions. Last, the sample is coated in 65 nm of Au, a necessary transducer layer for FDTR. The fabrication of a second sample to ensure reproducibility follows a similar procedure without the Cr wedge deposition step. The deposition pressures of the two samples are 10<sup>−9</sup> and 10<sup>−8</sup> Torr, respectively, at a rate of 0.2 nm/min.

In order to establish the equilibrium phases of the metals, the samples are annealed at 180 °C for 1 h after each deposition step.

**Material Characterization.** The thicknesses of the metals and alloy composition as a function of space are determined by EDX spectroscopy. The thickness map of Ni, as an example, and the alloy composition map are available in the Supporting Information. The Ni wedge shows a relatively linear thickness gradient primarily in one direction. Because of a small spatial offset between the positioning of the graphene sample and the positions of the wedges, the alloy composition ranges from 0 to 70 at. % Pd in Ni.

The EDX system uses a Tescan scanning electron microscope equipped with an Oxford Instruments X-max 80 mm<sup>2</sup> detector. The thicknesses are mapped across a 9 mm × 9 mm area centered on the graphene with a 1 mm grid spacing. The 0–10 keV EDX spectra are recorded by rastering a 20 keV electron beam across a 50 × 50 μm area at each point. Thicknesses are extracted through spectra fitting done by INCA ThinFilmID software. The fitting procedure models the layers as Au, Ni–Pd CSAF, Cr (excluded for the second sample), and graphene on a SiO<sub>2</sub>/Si substrate.

**Thermal Characterization.** The optical pump–probe technique, FDTR,<sup>59</sup> is used to measure  $G$  as a function of alloy composition and Cr thickness in contact with graphene. FDTR measurements are collected at positions on the sample corresponding with EDX measurement locations, with linearly interpolated locations also being measured in order to report higher-resolution thermal data than composition data. Linear interpolation is appropriate because the spatial thickness gradient of the deposited metal wedges is also linear.

The FDTR phase lag data between the reflected pump and probe beams are collected for 20 logarithmically spaced pump modulation frequencies between 300 kHz and 5 MHz. The data are then fit to a solution of the heat diffusion equation for a layered structure<sup>37</sup> composed of Au, Ni–Pd alloy, Cr (excluded for the second sample), the junction interface of interest, 90 nm of SiO<sub>2</sub>, and Si. The junction of interest represents the monolayer graphene and its two adjacent interfaces.

The vertical error bars of our  $G$  data represent the first and third quartiles in the distribution of  $G$  for each alloy composition, resulting from the Monte Carlo method of randomly generating sets of fitting parameter values from normal distributions of each.<sup>60</sup> Further details of the FDTR fitting and example histograms of the Monte Carlo method used for uncertainty analysis can be found in the Supporting Information.

## ASSOCIATED CONTENT

### Supporting Information

The Supporting Information is available free of charge at <https://pubs.acs.org/doi/10.1021/acsami.0c06953>.

Ni–Pd binary phase diagram, thermal conductivity of Ni–Pd alloy thin films, FDTR uncertainty analysis, EDX

mapping of alloy thin films, and Raman spectroscopy of graphene (PDF)

## AUTHOR INFORMATION

### Corresponding Author

**Jonathan A. Malen** – Department of Mechanical Engineering, Carnegie Mellon University, Pittsburgh, Pennsylvania 15213, United States; [orcid.org/0000-0003-4560-4476](https://orcid.org/0000-0003-4560-4476); Email: [jonmalen@andrew.cmu.edu](mailto:jonmalen@andrew.cmu.edu)

### Authors

**Dipanjan Saha** – Department of Mechanical Engineering, Carnegie Mellon University, Pittsburgh, Pennsylvania 15213, United States

**Xiaoxiao Yu** – Department of Chemical Engineering, Carnegie Mellon University, Pittsburgh, Pennsylvania 15213, United States

**Yanhao Du** – Department of Electrical and Computer Engineering, University of Pittsburgh, Pittsburgh, Pennsylvania 15261, United States

**Zhitao Guo** – Department of Chemical Engineering, Carnegie Mellon University, Pittsburgh, Pennsylvania 15213, United States

**Feng Xiong** – Department of Electrical and Computer Engineering, University of Pittsburgh, Pittsburgh, Pennsylvania 15261, United States

**Andrew J. Gellman** – Department of Chemical Engineering and W. E. Scott Institute for Energy Innovation, Carnegie Mellon University, Pittsburgh, Pennsylvania 15213, United States; [orcid.org/0000-0001-6618-7427](https://orcid.org/0000-0001-6618-7427)

Complete contact information is available at:

<https://pubs.acs.org/10.1021/acsami.0c06953>

### Author Contributions

D.S.: writing, metal deposition, EDX, thermal characterization, electrical device fabrication, electrical characterization, Raman spectroscopy, TEM analysis, 4-point probe device fabrication/measurements. X.Y.: metal deposition, EDX. Z.G.: metal deposition, EDX. Y.D.: electrical device design/fabrication, electrical characterization, Raman spectroscopy

### Notes

The authors declare no competing financial interest.

## ACKNOWLEDGMENTS

We would like to acknowledge the contributions of Mohamed Darwish with Raman spectroscopy and designing our four-point probe devices and Yunus Kesim with fabricating/measuring these devices. We would also like to acknowledge the contributions of Noel Tom Nuhfer in the Material Characterization Facility at Carnegie Mellon University toward the cross-sectional HRTEM images presented in this publication. D.S. and J.A.M. acknowledge the support from the National Science Foundation ENG ECCS 1901972 and Army Research Office Grant W911NF-17-1-0397. Y.D. and F.X. acknowledge the support from NSF ENG ECCS 1901864 and MCSI Seed Fund from University of Pittsburgh. X.Y. and A.G. acknowledge the support from NSF-CHE1566228. This work was performed, in part, at the Nanoscale Fabrication and Characterization Facility, a laboratory of the Gertrude E. and John M. Petersen Institute of NanoScience and Engineering, housed at the University of Pittsburgh.

## REFERENCES

- (1) Geim, A. K.; Novoselov, K. S. The Rise of Graphene. *Nat. Mater.* **2007**, *6*, 183–191.
- (2) Novoselov, K. S.; Fal'ko, V. I.; Colombo, L.; Gellert, P. R.; Schwab, M. G.; Kim, K. A Roadmap for Graphene. *Nature* **2012**, *490*, 192–200.
- (3) Chen, Z.; Jang, W.; Bao, W.; Lau, C. N.; Dames, C. Thermal Contact Resistance between Graphene and Silicon Dioxide. *Appl. Phys. Lett.* **2009**, *95*, 161910.
- (4) Hsu, A.; Wang, H.; Kim, K. K.; Kong, J.; Palacios, T. Impact of Graphene Interface Quality on Contact Resistance and RF Device Performance. *IEEE Electron Device Lett.* **2011**, *32*, 1008–1010.
- (5) Watanabe, E.; Conwill, A.; Tsuya, D.; Koide, Y. Low Contact Resistance Metals for Graphene Based Devices. *Diamond Relat. Mater.* **2012**, *24*, 171–174.
- (6) Nagashio, K.; Nishimura, T.; Kita, K.; Toriumi, A. Metal/Graphene Contact as a Performance Killer of Ultra-High Mobility Graphene—Analysis of Intrinsic Mobility and Contact Resistance. *Technical Digest—International Electron Devices Meeting*, 2009, pp 1–4.
- (7) Bae, M.-H.; Ong, Z.-Y.; Estrada, D.; Pop, E. Imaging, Simulation, and Electrostatic Control of Power Dissipation in Graphene Devices. *Nano Lett.* **2010**, *10*, 4787–4793.
- (8) Yu, Y.-J.; Han, M. Y.; Berciaud, S.; Georgescu, A. B.; Heinz, T. F.; Brus, L. E.; Kim, K. S.; Kim, P. High-Resolution Spatial Mapping of the Temperature Distribution of a Joule Self-Heated Graphene Nanoribbon. *Appl. Phys. Lett.* **2011**, *99*, 183105.
- (9) Freitag, M.; Chiu, H.-Y.; Steiner, M.; Perebeinos, V.; Avouris, P. Thermal Infrared Emission from Biased Graphene. *Nat. Nanotechnol.* **2010**, *5*, 497–501.
- (10) Balandin, A. A.; Ghosh, S.; Bao, W.; Calizo, I.; Teweldebrhan, D.; Miao, F.; Lau, C. N. Superior Thermal Conductivity of Graphene. *Nano Lett.* **2008**, *8*, 902–907.
- (11) Koh, Y. K.; Bae, M.-H.; Cahill, D. G.; Pop, E. Heat Conduction across Monolayer and Few-Layer Graphenes. *Nano Lett.* **2010**, *10*, 4363–4368.
- (12) Tewary, V. K.; Yang, B. Singular Behavior of the Debye-Waller Factor of Graphene. *Phys. Rev. B: Condens. Matter Mater. Phys.* **2009**, *79*, 125416.
- (13) Vasquez Guzman, P. A.; Sood, A.; Mleczko, M. J.; Wang, B.; Wong Philip, H. S.; Nishi, Y.; Asheghi, M.; Goodson, K. E. Cross Plane Thermal Conductance of Graphene-Metal Interfaces. *Fourteenth Intersociety Conference on Thermal and Thermomechanical Phenomena in Electronic Systems (ITherm)*, 2014, pp 1385–1389.
- (14) Foley, B. M.; Hernández, S. C.; Duda, J. C.; Robinson, J. T.; Walton, S. G.; Hopkins, P. E. Modifying Surface Energy of Graphene via Plasma-Based Chemical Functionalization to Tune Thermal and Electrical Transport at Metal Interfaces. *Nano Lett.* **2015**, *15*, 4876–4882.
- (15) Hopkins, P. E.; Baraket, M.; Barnat, E. V.; Beechem, T. E.; Kearney, S. P.; Duda, J. C.; Robinson, J. T.; Walton, S. G. Manipulating Thermal Conductance at Metal-Graphene Contacts via Chemical Functionalization. *Nano Lett.* **2012**, *12*, 590–595.
- (16) Zheng, W.; Huang, B.; Li, H.; Koh, Y. K. Achieving Huge Thermal Conductance of Metallic Nitride on Graphene Through Enhanced Elastic and Inelastic Phonon Transmission. *ACS Appl. Mater. Interfaces* **2018**, *10*, 35487–35494.
- (17) Samani, M. K.; Ding, X. Z.; Khosravian, N.; Amin-Ahmadi, B.; Yi, Y.; Chen, G.; Neyts, E. C.; Bogaerts, A.; Tay, B. K. Thermal Conductivity of Titanium Nitride/Titanium Aluminum Nitride Multilayer Coatings Deposited by Lateral Rotating Cathode Arc. *Thin Solid Films* **2015**, *578*, 133–138.
- (18) Nagareddy, V. K.; Nikitina, I. P.; Gaskill, D. K.; Tedesco, J. L.; Myers-Ward, R. L.; Eddy, C. R.; Goss, J. P.; Wright, N. G.; Horsfall, A. B. High Temperature Measurements of Metal Contacts on Epitaxial Graphene. *Appl. Phys. Lett.* **2011**, *99*, 073506.
- (19) Khomyakov, P. A.; Giovannetti, G.; Rusu, P. C.; Brocks, G.; Van Den Brink, J.; Kelly, P. J. First-Principles Study of the Interaction and Charge Transfer between Graphene and Metals. *Phys. Rev. B: Condens. Matter Mater. Phys.* **2009**, *79*, 195425.

- (20) Giovannetti, G.; Khomyakov, P. A.; Brocks, G.; Karpan, V. M.; Van Den Brink, J.; Kelly, P. J. Doping Graphene with Metal Contacts. *Phys. Rev. Lett.* **2008**, *101*, 026803.
- (21) Quiroga, M. A. O.; Cabeza, G. F. Role of Van Der Waals Forces in Graphene Adsorption over Pd, Pt, and Ni. *Braz. J. Phys.* **2013**, *43*, 126–129.
- (22) Hu, L.; Hu, X.; Wu, X.; Du, C.; Dai, Y.; Deng, J. Density Functional Calculation of Transition Metal Adatom Adsorption on Graphene. *Phys. Rev. B: Condens. Matter Mater. Phys.* **2010**, *40S*, 3337–3341.
- (23) Kozlov, S. M.; Viñes, F.; Görling, A. Bonding Mechanisms of Graphene on Metal Surfaces. *J. Phys. Chem. C* **2012**, *116*, 7360–7366.
- (24) Mao, R.; Kong, B. D.; Gong, C.; Xu, S.; Jayasekera, T.; Cho, K.; Kim, K. W. First-Principles Calculation of Thermal Transport in Metal/Graphene Systems. *Phys. Rev. B: Condens. Matter Mater. Phys.* **2013**, *87*, 165410.
- (25) Valencia, H.; Gil, A.; Frapper, G. Trends in the Adsorption of 3d Transition Metal Atoms onto Graphene and Nanotube Surfaces: A DFT Study and Molecular Orbital Analysis. *J. Phys. Chem. C* **2010**, *114*, 14141–14153.
- (26) Jeong, M.; Freedman, J. P.; Liang, H. J.; Chow, C. M.; Sokalski, V. M.; Bain, J. A.; Malen, J. A. Enhancement of Thermal Conductance at Metal-Dielectric Interfaces Using Subnanometer Metal Adhesion Layers. *Phys. Rev. Appl.* **2016**, *5*, 014009.
- (27) Robinson, J. A.; Labella, M.; Zhu, M.; Hollander, M.; Kasarda, R.; Hughes, Z.; Trumbull, K.; Cavallero, R.; Snyder, D. Contacting Graphene. *Appl. Phys. Lett.* **2011**, *98*, 053103.
- (28) Huang, B.-C.; Zhang, M.; Wang, Y.; Woo, J. Contact Resistance in Top-Gated Graphene Field-Effect Transistors. *Appl. Phys. Lett.* **2011**, *99*, 032107.
- (29) Song, S. M.; Park, J. K.; Sul, O. J.; Cho, B. J. Determination of Work Function of Graphene under a Metal Electrode and Its Role in Contact Resistance. *Nano Lett.* **2012**, *12*, 3887–3892.
- (30) Blake, P.; Yang, R.; Morozov, S. V.; Schedin, F.; Ponomarenko, L. A.; Zhukov, A. A.; Nair, R. R.; Grigorieva, I. V.; Novoselov, K. S.; Geim, A. K. Influence of Metal Contacts and Charge Inhomogeneity on Transport Properties of Graphene near the Neutrality Point. *Solid State Commun.* **2009**, *149*, 1068–1071.
- (31) Franklin, A. D.; Han, S.-J.; Bol, A. A.; Perebeinos, V. Double Contacts for Improved Performance of Graphene Transistors. *IEEE Electron Device Lett.* **2012**, *33*, 17–19.
- (32) Lin, C. J.; Gorman, G. L. Evaporated CoPt Alloy Films with Strong Perpendicular Magnetic Anisotropy. *Appl. Phys. Lett.* **1992**, *61*, 1600–1602.
- (33) Santala, T.; Adams, C. M. Kinetics and Thermodynamics in Continuous Electron-Beam Evaporation of Binary Alloys. *J. Vac. Sci. Technol.* **1970**, *7*, S22–S29.
- (34) Powell, A.; Pal, U.; van den Avyle, J.; Damkroger, B.; Szekeley, J. Analysis of Multicomponent Evaporation in Electron Beam Melting and Refining of Titanium Alloys. *Metall. Mater. Trans. B* **1997**, *28*, 1227–1239.
- (35) SGTE Solder Alloy Phase Diagrams [http://www.crct.polymtl.ca/fact/phase\\_diagram.php?file=Ni-Pd.jpg&dir=SGsold](http://www.crct.polymtl.ca/fact/phase_diagram.php?file=Ni-Pd.jpg&dir=SGsold) (accessed Jan 27, 2017).
- (36) Bale, C. W.; Bêlisle, E.; Chartrand, P.; Decterov, S. A.; Eriksson, G.; Gheribi, A. E.; Hack, K.; Jung, I.-H.; Kang, Y.-B.; Melançon, J.; Pelton, A. D.; Petersen, S.; Robelin, C.; Sangster, J.; Van Ende, M.-A. *FactSage Thermochemical Software and Databases, 2010–2016* [www.factsage.com](http://www.factsage.com).
- (37) Cahill, D. G. Analysis of Heat Flow in Layered Structures for Time-Domain Thermoreflectance. *Rev. Sci. Instrum.* **2004**, *75*, S119–S122.
- (38) Saha, D.; Yu, X.; Jeong, M.; Darwish, M.; Weldon, J.; Gellman, A. J.; Malen, J. A. Impact of Metal Adhesion Layer Diffusion on Thermal Interface Conductance. *Phys. Rev. B* **2019**, *99*, 115418.
- (39) Nash, A.; Nash, P. The Ni-Pd (Nickel-Palladium) System. *Bull. Alloy Phase Diagrams* **1984**, *5*, 446–450.
- (40) Fraenkel, W.; Stern, A. Des System Palladium-Nickel. *Z. Anorg. Chem.* **1927**, *166*, 164–165.
- (41) Lin, W.; Spruiell, J. E. The Structure of Nickel-Palladium Solid Solutions. *Acta Metall.* **1971**, *19*, 451–461.
- (42) Hultgren, R.; Zapffe, C. A. An X-Ray Study of the Iron-Palladium and Nickel-Palladium Systems. *Trans. AIME* **1939**, *133*, 58–68.
- (43) Androulakis, J.; Lin, C.-H.; Kong, H.-J.; Uher, C.; Wu, C.-I.; Hogan, T.; Cook, B. A.; Caillat, T.; Paraskevopoulos, K. M.; Kanatzidis, M. G. Spinodal Decomposition and Nucleation and Growth as a Means to Bulk Nanostructured Thermoelectrics: Enhanced Performance in  $\text{Pb}_{1-x}\text{Sn}_x\text{Te}-\text{PbS}$ . *J. Am. Chem. Soc.* **2007**, *129*, 9780–9788.
- (44) Huston, E. L.; Cahn, J. W.; Hilliard, J. E. Spinodal Decomposition during Continuous Cooling. *Acta Metall.* **1966**, *14*, 1053–1062.
- (45) Leong, W. S.; Nai, C. T.; Thong, J. T. L. What Does Annealing Do to Metal-Graphene Contacts? *Nano Lett.* **2014**, *14*, 3840–3847.
- (46) Leong, W. S.; Gong, H.; Thong, J. T. L. Low-Contact-Resistance Graphene Devices with Nickel-Etched-Graphene Contacts. *ACS Nano* **2014**, *8*, 994–1001.
- (47) Kimling, J.; Philippi-Kobs, A.; Jacobsohn, J.; Oepen, H. P.; Cahill, D. G. Thermal Conductance of Interfaces with Amorphous  $\text{SiO}_2$  Measured by Time-Resolved Magneto-Optic Kerr-Effect Thermometry. *Phys. Rev. B* **2017**, *95*, 184305.
- (48) Norimatsu, W.; Kusunoki, M. Epitaxial Graphene on  $\text{SiC}\{0001\}$ : Advances and Perspectives. *Phys. Chem. Chem. Phys.* **2014**, *16*, 3501–3511.
- (49) Yu, W. J.; Li, Z.; Zhou, H.; Chen, Y.; Wang, Y.; Huang, Y.; Duan, X. Vertically Stacked Multi-Heterostructures of Layered Materials for Logic Transistors and Complementary Inverters. *Nat. Mater.* **2013**, *12*, 246–252.
- (50) Wang, K.; Tai, G.; Wong, K. H.; Lau, S. P.; Guo, W. Ni Induced Few-Layer Graphene Growth at Low Temperature by Pulsed Laser Deposition. *AIP Adv.* **2011**, *1*, 022141.
- (51) Sato, M.; Inukai, M.; Ikenaga, E.; Muro, T.; Ogawa, S.; Takakuwa, Y.; Nakano, H.; Kawabata, A.; Nihei, M.; Yokoyama, N. Fabrication of Graphene Directly on  $\text{SiO}_2$  without Transfer Processes by Annealing Sputtered Amorphous Carbon. *Jpn. J. Appl. Phys.* **2012**, *51*, 04DB01.
- (52) Kato, T.; Hatakeyama, R. Site- and Alignment-Controlled Growth of Graphene Nanoribbons from Nickel Nanobars. *Nat. Nanotechnol.* **2012**, *7*, 651–656.
- (53) Anzi, L.; Mansouri, A.; Pedrinazzi, P.; Guerriero, E.; Fiocco, M.; Pesquera, A.; Centeno, A.; Zurutuza, A.; Behnam, A.; Carrion, E. A.; Pop, E.; Sordan, R. Ultra-Low Contact Resistance in Graphene Devices at the Dirac Point. *2D Mater.* **2018**, *5*, 025014.
- (54) Kumar, K.; Kim, Y.-S.; Yang, E.-H. The Influence of Thermal Annealing to Remove Polymeric Residue on the Electronic Doping and Morphological Characteristics of Graphene. *Carbon* **2013**, *65*, 35–45.
- (55) Choi, W.; Seo, Y.-S.; Park, J.-Y.; Kim, K. B.; Jung, J.; Lee, N.; Seo, Y.; Hong, S. Effect of Annealing in  $\text{Ar}/\text{H}_2$  Environment on Chemical Vapor Deposition-Grown Graphene Transferred with Poly (Methyl Methacrylate). *IEEE Trans. Nanotechnol.* **2015**, *14*, 70–74.
- (56) Lin, Y.-C.; Lu, C.-C.; Yeh, C.-H.; Jin, C.; Suenaga, K.; Chiu, P.-W. Graphene Annealing: How Clean Can It Be? *Nano Lett.* **2012**, *12*, 414–419.
- (57) Fleutot, B.; Miller, J. B.; Gellman, A. J. Apparatus for Deposition of Composition Spread Alloy Films: The Rotatable Shadow Mask. *J. Vac. Sci. Technol., A* **2012**, *30*, 061511.
- (58) Yu, X.; Gellman, A. J. Suppression of B2 Phase in  $\text{PdZrCu}_{1-x}$  Alloy Thin Films. *Thin Solid Films* **2018**, *668*, 50–55.
- (59) Schmidt, A. J.; Cheaito, R.; Chiesa, M. A Frequency-Domain Thermoreflectance Method for the Characterization of Thermal Properties. *Rev. Sci. Instrum.* **2009**, *80*, 094901.
- (60) Bougher, T. L.; Yates, L.; Lo, C.-F.; Johnson, W.; Graham, S.; Cola, B. A. Thermal Boundary Resistance in GaN Films Measured by Time Domain Thermoreflectance with Robust Monte Carlo Uncertainty Estimation. *Nanoscale Microscale Thermophys. Eng.* **2016**, *20*, 22–32.